Relaying alkaline hydrogen evolution over locally amorphous Ni/Co-based phosphides constructed by diffusion-limited phase-transition

Ke Wang [a,1], Song He [a,1], Boxin Li [a], Hongfang Du [b,*], Tingfeng Wang [a], Zhuzhu Du [a], Linghai Xie [c], Wei Ai [a,*]

[a] *Frontiers Science Center for Flexible Electronics (FSCFE) and Shaanxi Institute of Flexible Electronics (SIFE), Northwestern Polytechnical University, 127 West Youyi Road, Xi'an 710072, China*
[b] *Strait Laboratory of Flexible Electronics (SLoFE), Strait Institute of Flexible Electronics (SIFE, Future Technologies), Fujian Normal University, Fuzhou 350117, China*
[c] *Key Laboratory of Organic Electronics and Information Displays (KLOFE) & Institute of Advanced Materials (IAM), Nanjing University of Posts & Telecommunications, 9 Wenyuan Road, Nanjing 210023, China*

ARTICLE INFO

ABSTRACT

Ni/Co-based phosphides are a family of promising electrocatalysts for hydrogen evolution reaction (HER), but the sluggish water dissociation kinetics impedes their applications in alkaline condition. Herein, locally amorphous NiCoP (LA-NiCoP) with enhanced orbital coupling to facilitate water dissociation is constructed by a low-temperature molten salt enabled diffusion-limited phase-transition strategy. Time-dependent experiment systematically clarifies the crystallinity regulation mechanism of NiCoP associated with its nonclassical crystallization process of amorphous-to-crystalline transition. As the alkaline HER electrocatalyst, LA-NiCoP exhibits a close to Pt/C activity ($\eta_{10} = 45$ mV). Both experimental and theoretical results show that the Co atoms in the amorphous phase display higher proportion of unoccupied 3d orbitals than the crystalline counterpart, which interacts with the O 2p of H_2O for activating the cleavage of HO–H bond. This work not only provides a facile approach to prepare locally amorphous phosphides, but also offers a new protocol to accelerate the water dissociation kinetics.

1. Introduction

Owing to their moderate hydrogen binding energy, Ni/Co-based phosphides (NCPs) have been emerging as low-cost hydrogen evolution reaction (HER) electrocatalysts in acidic media [1–4]. However, NCPs generally suffer from insufficient proton supply in alkaline solution due to the sluggish water dissociation process [5–8]. On the basis of molecular orbital theory, the metal atoms in NCPs are considered as the adsorption and dissociation sites of water by electron coupling between the 3d orbital of metal atoms and 2p orbital of oxygen atom in water [9,10]. In view of the inherently low proportion of unoccupied 3d orbital in Ni and Co, their orbital overlapping with water is very limited due to the Pauli repulsion [11,12]. With the poor water dissociation kinetics, the alkaline HER activity of NCPs is two to three orders of magnitude lower than that in acidic electrolyte [13,14]. Given that alkaline media are compatible with non-noble metal catalysts for oxygen evolution reaction [15,16], enormous efforts have been devoted to lowing the energy barrier of NCPs for water dissociation.

Coupling NCPs with oxophilic species, such as transition metal oxides and hydroxides, can accelerate the water dissociation kinetics and thereby facilitates the Volmer step of alkaline HER [8,17]. Unfortunately, under HER potential, these extraneous oxophilic compounds are readily deactivated because of their reduction to low-valence species, leading to unsatisfactory durability [18–20]. Alternatively, introducing heteroatoms or constructing heterostructures can achieve dual sites on NCPs to separately adsorb the OH* and H* intermediates of HER, which synergistically promotes the cleavage of the HO–H bond [21–23]. However, with limited choice of suitable materials, it remains a big challenge to achieve the good balance between electrochemical performance and composite compatibility [24]. It is recently reported that the amorphization of nanomaterials can induce abundant dangling bonds with flexible electron configurations, consequently more frequent orbital coupling to promote alkaline water splitting [25–27]. In this regard, it is expected that the local amorphization of NCPs, meaning,
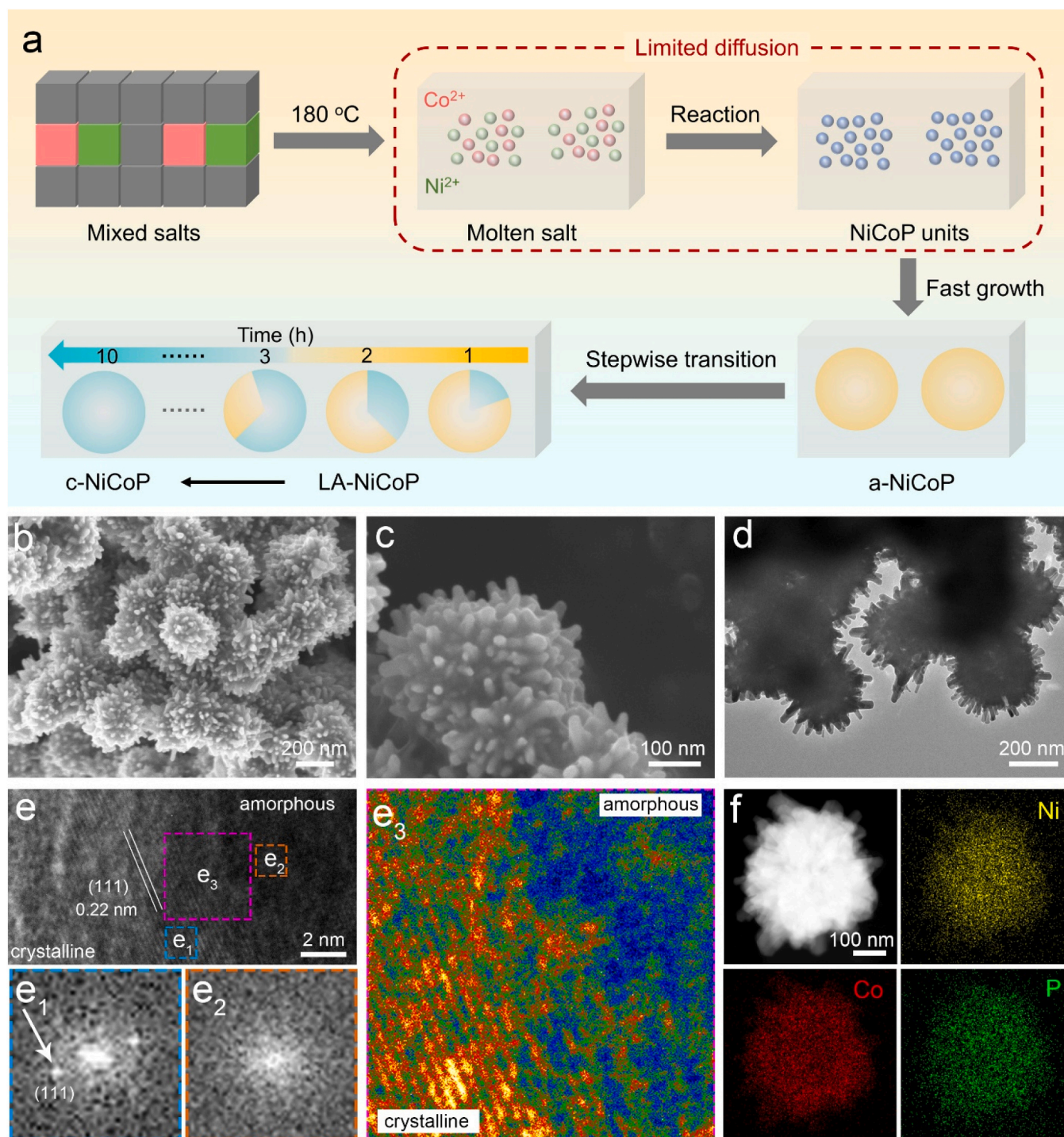
Fig. 1. (a) Schematic illustration of the formation of LA-NiCoP. (b, c) SEM, (d) TEM, and (e) HRTEM images of LA-NiCoP. The corresponding (e$_1$, e$_2$) FFT and (e$_3$) inverse FFT patterns of the selected regions in e, which are marked by the blue, orange and pink squares, respectively. (f) HAADF-STEM and the corresponding EDS mapping images of LA-NiCoP.

introducing amorphous phase to manipulate the proportion of unoccupied 3d orbital of metal atoms while preserving the intrinsic hydrogen binding features of the crystalline phase, may accelerate the water dissociation kinetics dramatically. Nevertheless, owing to the lack of reliable synthesis methods, to date, NCPs are synthesized either amorphous or crystalline, and the structure-property relationships of local amorphization have yet been elusive [2,3].

Herein, we report a low-temperature molten salt approach to construct locally amorphous NiCoP (LA-NiCoP), where the unique

phosphatization environment with high viscosity enables fast growth and stepwise crystallization of NiCoP units to obtain the coexistence of amorphous and crystalline phases. Time-dependent experiment suggests the diffusion-limited amorphous-to-crystalline transition of NiCoP, through which the amorphization degree could be easily controlled. Moreover, this strategy is also applicable to the other NCPs, for example, Ni$_{12}$P$_5$ and Co$_2$P, as demonstrated in our case studies. Among them, LA-NiCoP exhibits the best HER activity in terms of a small η_{10} of 45 mV and a η_{200} of 131 mV in 1.0 M KOH, which is close to the benchmark Pt/C

and significantly outperforms the state-of-art NCPs electrocatalysts. Density functional theory (DFT) calculations state that the amorphous phase showing a higher proportion of unoccupied 3d orbitals favors water adsorption and dissociation to promote the Volmer reaction, whilst the crystalline phase with moderate hydrogen binding energy benefits the afore-produced H* adsorption/desorption to accelerate the Heyrovsky reaction.

2. Experimental section

2.1. Synthesis of LA-NiCoP

0.089 g Ni(CH$_3$COO)$_2$, 0.089 g Co(CH$_3$COO)$_2$ and 8.8 g NaH$_2$PO$_2$ was mixed in a closed vessel, and then heated to 180 °C for 2 h. After cooling down to room temperature naturally, LA-NiCoP was obtained by washing the product with deionized water and subsequently dried in a vacuum oven at 60 °C for 6 h. LA-NiCoP with different crystallinities were prepared by tuning the reaction time (1, 2, 3, and 10 h), while a-NiCoP was synthesized at a reaction peroid of 1 min. The LA-Ni$_{12}$P$_5$ and LA-Co$_2$P were synthesized under the similar experimental procedures by heating Ni(CH$_3$COO)$_2$ or Co(CH$_3$COO)$_2$ with NaH$_2$PO$_2$. The molar ratio of phosphorus and metal precursors is controlled to be about 100:1, according to our previous work of molten salt synthesizing transition metal sulfides [28].

2.2. Characterizations

The surface structures of the samples were investigated using a field emission scanning electron microscope (FEI Verios G4) operated at an accelerating voltage of 10 kV. XPS characterization was conducted on a Kratos AXIS Ultra DLD. XRD data were recorded on a Bruker D8 ADVANCE Diffractometer with Cu Kα radiation (λ = 1.54056 Å). TEM measurements and related EDS analysis were carried on a FEI TECNAI G2 F20 with an accelerating voltage of 200 kV. EPR spectra were collected on a Bruker EMXplus spectrometer.

2.3. Electrochemical measurements

Electrochemical measurements were conducted on a CHI 760e electrochemical workstation. A typical three-electrode electrolyzer was used, including a piece of carbon paper (0.5 × 0.5 cm^2) as the working electrode, a graphite rod as the counter electrode, a Hg/HgO electrode as the reference electrode in 1.0 M KOH. For acidic HER tests, a saturated calomel electrode (SCE) was used as the reference electrode. For the preparation of catalyst ink, 10 mg catalyst was dispersed in 250 μL ethanol containing 15 μL Nafion (5 wt%), followed by treating in an ultrasonic bath for 15 min to get a homogeneous mixture. After then, 12.5 μL of the ink was transferred to carbon paper and dried at room temperature. The polarization curves were obtained at a scan rate of 5 mV s^{-1}. Nyquist plots were acquired under an overpotential of 30 mV in a frequency range of 10^{-1}~10^5 Hz with an AC amplitude of 5 mV. Durability was evaluated by continuous CV cycling (–0.2–0 V, 100 mV s^{-1}) and Chronopotentiometry curves (10 mA cm^{-2}). All potentials were calibrated to the reversible hydrogen electrode (RHE) scale according to the Nernst equation: $E_{RHE} = E_{SCE} + 0.059$ pH $+ 0.098$ and $E_{RHE} = E_{SCE} + 0.059$ pH $+ 0.242$ in 1.0 M KOH and 0.5 M H$_2$SO$_4$, respectively. All electrochemical data were *i*R-corrected.

2.4. Computational methods

First-principles were employed to perform the spin-polarization DFT calculations within the generalized gradient approximation using the Perdew-Burke-Ernzerhof formulation [29,30]. The projected augmented wave potentials were selected to describe the ionic cores and take valence electrons into account using a plane wave basis set with a kinetic energy cutoff of 450 eV. Partial occupancies of the Kohn-Sham orbitals

were allowed using the Gaussian smearing method with a width of 0.05 eV. The electronic energy was considered self-consistent when the energy change was less than 10^{-4} eV. A geometry optimization was considered convergent when the energy change was less than 0.05 eV Å^{-1}.

To model a realistic amorphous NiCoP with short-range ordered structure, the NVT (the amount of substance (N), volume (V) and temperature (T)) ensemble was used for ab-initio molecular dynamics (AIMD) simulation to conduct an anneal-to-quench process. The NiCoP structure was optimized by using a time step of 1 fs in the NVT ensemble. Finally, it was relaxed using DFT calculations. The cutoff energy of the plane-wave basis was set to 400 eV in the relaxation while 300 eV was used in the AIMD simulations. 1 × 1 × 1 Gamma-centered k-mesh is used in relaxation and AIMD simulations. Time step in AIMD is set to be 1 femtosecond, Nose-Hoover thermostat is used to keep temperature (statistically) constant at 1000 K with 20 ps.

The adsorption energies (E$_{ads}$) were calculated as: E$_{ads}$ = E$_{ad/sub}$ – E$_{ad}$ – E$_{sub}$, where E$_{ad/sub}$, E$_{ad}$, and E$_{sub}$ are the total energies of the optimized adsorbate/substrate system, the adsorbate in the gas phase, and the clean substrate, respectively. The Brillouin zone integral was sampled using the surfaces structures of 2 × 2 × 1 Monkhorst-Pack *k* point for the structural optimization. The free energies for elemental reaction steps were calculated as: G = E + ZPE – TS, where G, E, ZPE and TS are the free energy, total energy, zero point energy and entropy contribution (T = 300 K), respectively.

3. Results and discussion

3.1. Synthesis and characterization of LA-NiCoP

LA-NiCoP was prepared by heating the mixture of Ni(CH$_3$COO)$_2$, Co(CH$_3$COO)$_2$ and NaH$_2$PO$_2$ at a low temperature of 180 °C for 2 h (for more details, please see Experimental Section). As both the reaction medium and phosphorus source, NaH$_2$PO$_2$ molten salt affords a unique phosphatization environment with high viscosity, which results in the sluggish diffusion of metal ions and the subsequently generated NiCoP units during the reaction [31]. The slow molecular motion makes it difficult to crystallize NiCoP by means of the classical crystallization due to the high kinetic barrier [32–34]. Instead, a nonclassical crystallization process of amorphous-to-crystalline transition is achieved, forming LA-NiCoP [35–37]. As schematically shown in Fig. 1a, upon initiating the reaction, NiCoP units would be instantly produced and fast growth to form large-sized nanoparticles with amorphous structure (Fig. S1) [38, 39]. According to Ostwald step rule, the amorphous NiCoP (a-NiCoP) with metastable structure would stepwise transform to crystalline NiCoP (c-NiCoP) via structural relaxation [36,40]. With moderate reaction time, locally amorphous nanostructure would be obtained. Scanning electron microscopy (SEM) and transmission electron microscopy (TEM) images show that the as-synthesized LA-NiCoP exhibits a massaging ball-like structure (Fig. 1b–d). The high-resolution TEM (HRTEM) images in Fig. 1e and S2 show that LA-NiCoP is constituted by crystalline and amorphous domains, in which a clear lattice fringe with a spacing of 0.22 nm is indexed to the (111) crystal plane of NiCoP [41]. This is further supported by the bright spots (Fig. 1e$_1$) and diffuse ring (Fig. 1e$_2$) in the corresponding selected-area fast Fourier transform (FFT) patterns. In addition, the inverse FFT pattern in Fig. 1e$_3$ clearly corroborates the coexistence of crystalline and amorphous phases in LA-NiCoP. Fig. 1f displays the high-angle annular dark-field scanning transmission electron microscopy (HAADF-STEM) and the corresponding elemental mapping images of LA-NiCoP, illustrating the uniform distribution of Ni, Co and P elements throughout the sample. Based on energy dispersive spectroscopy (EDS) analysis (Fig. S3), the atomic ratio of Ni, Co, and P elements is determined to be about 1:1:1, consistent with the stoichiometric ratio of NiCoP.

To verify this diffusion-limited phase-transition mechanism, time-controlled synthesis was performed by tuning the reaction time
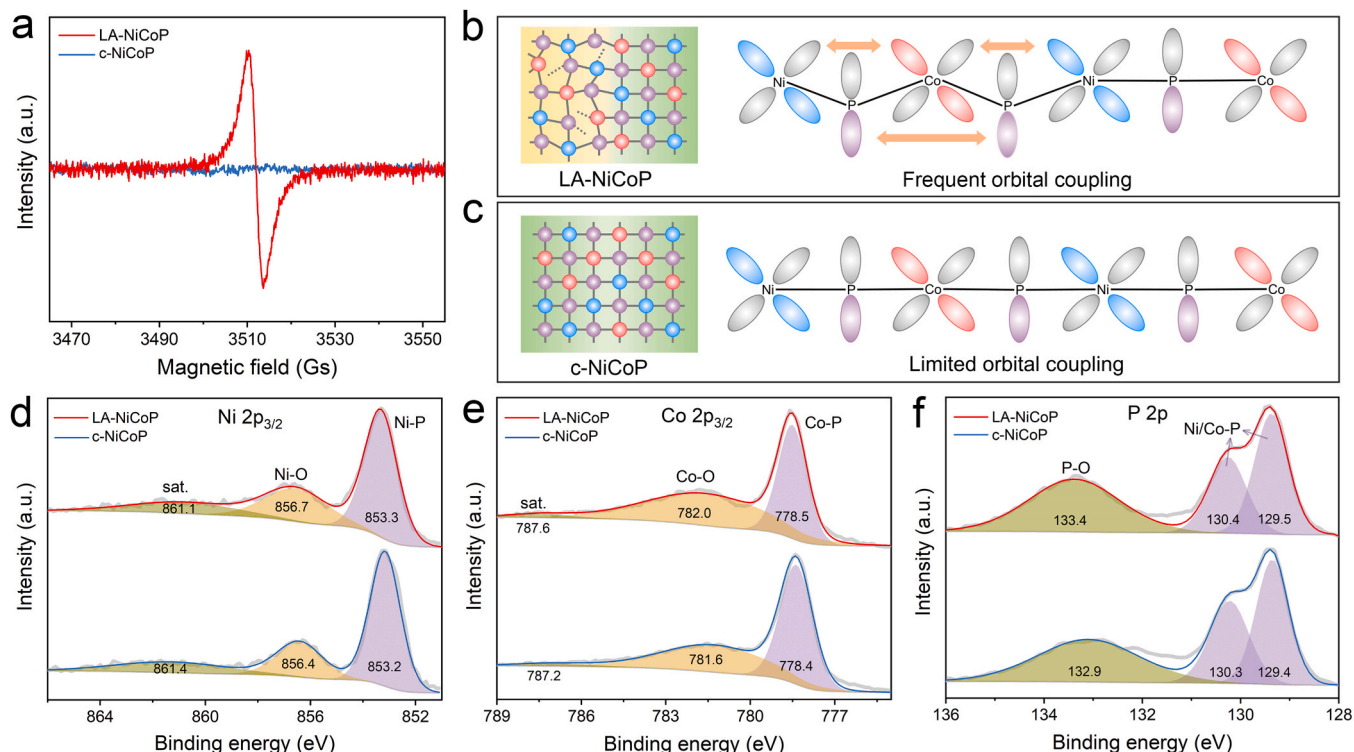
Fig. 2. (a) EPR spectra of LA-NiCoP and c-NiCoP. Schematic representations of the structure and electronic coupling for (b) LA-NiCoP and (c) c-NiCoP. High-resolution (d) Ni 2p$_{3/2}$, (e) Co 2p$_{3/2}$, and (f) P 2p XPS spectra of LA-NiCoP and c-NiCoP.

(Fig. S4). SEM and TEM images illustrate that the overall structure of the samples is analogous to each other, however, the crystallinity increases significantly with prolonging the reaction time. As revealed by the HRTEM images, the gradually increased crystalline domains corroborate the stepwise crystallization of NiCoP through an amorphous-to-crystalline transition process. This is further evidenced by powder X-ray diffraction (XRD) patterns shown in Fig. S5. With an extended reaction time of 10 h, c-NiCoP was fabricated [42]. Such unique characteristics offer an exclusive opportunity to study the local amorphization of NCPs for boosting the HER performances. To better demonstrate the superiority of our methodology in the synthesis of locally amorphous NCPs, LA-Ni$_{12}$P$_5$ and LA-Co$_2$P were also prepared using Ni or Co salt in the reaction system with similar procedures (Figs. S6 and S7).

To reveal the role of the introduced amorphous phase in tuning the electron structure of NiCoP, electron paramagnetic resonance (EPR) spectra of LA-NiCoP and c-NiCoP were recorded (Fig. 2a). One can see that LA-NiCoP shows a pair of remarkable signals compared with c-NiCoP, indicating the presence of numerous unpaired electrons originated from the dangling bonds in the amorphous phase [43,44]. Actually, the abundant dangling bonds not only afford more accessible active sites for electrochemical reactions but also induce more frequent orbital coupling due to the flexible electronic structure (Fig. 2b and c) [25]. X-ray photoelectron spectroscopy (XPS) analysis was performed to uncover the chemical composition and bonding configuration of LA-NiCoP. As shown in Fig. S8, the signals for Ni, Co, and P elements are detected, consistent with the EDS results. In the high-resolution Ni 2p$_{3/2}$ spectrum (Fig. 2d), the prominent peak at 853.3 eV corresponds to the Ni–P, while the peaks at 856.7 and 861.1 eV are attributed to Ni–O and satellite peak, respectively [45,46]. The appearance of Ni–O is possibly caused by superficial oxidation of LA-NiCoP when exposing to air [47,48]. Likewise, the three peaks assignable to Co–P (778.5 eV), Co–O (782.0 eV), and satellite peak (787.6 eV) are also observed in the high-resolution Co 2p$_{3/2}$ spectrum (Fig. 2e) [49,50]. In the high-resolution P 2p region, the two peaks at 129.5 and 130.4 eV are ascribed to P 2p$_{3/2}$ and P 2p$_{1/2}$ of metal–P, while the peak at 133.4 eV is

assigned to the P–O (Fig. 2f) [51,52]. Compared with LA-NiCoP, the Ni 2p$_{3/2}$, Co 2p$_{3/2}$ and P 2p peaks in c-NiCoP shift to lower binding energy (Fig. 2d–f and S9), indicating the introduction of amorphous phase would bring higher oxidation state [53]. The metal sites with higher oxidation state may lead to stronger metal–O bonding because of the enhanced orbital overlap [54], which is beneficial for the adsorption and dissociation of H$_2$O.

3.2. Electrochemical performance of LA-NiCoP

The electrocatalytic performance of LA-NiCoP toward alkaline HER was investigated via a typical three-electrode configuration using 1.0 M KOH as the electrolyte (details in experimental section). Among them, the sample prepared at 2 h shows the best performance by virtue of its appropriate ratio of amorphous phase to crystalline phase (Figs. S4 and S10). For better comparison, the catalytic activities of a-NiCoP, c-NiCoP, and commercial Pt/C (20 %) were also tested. As shown in Fig. 3a, LA-NiCoP always requires a lower overpotential than a-NiCoP and c-NiCoP to achieve any current density, illustrating the great superiority of locally amorphous structure for alkaline HER. Importantly, the η_{10} and η_{200} of LA-NiCoP is determined to be 45 and 131 mV respectively, comparable to that of commercial Pt/C (42 and 163 mV). The Tafel slope was used to reveal the kinetics property of LA-NiCoP, a-NiCoP, and c-NiCoP [55], where the values are calculated to be 68, 76, and 81 mV dec^{-1}, respectively (Fig. 3b), indicating a Volmer-Heyrovsky HER process [56,57]. The smaller Tafel slope of LA-NiCoP suggests that it undergoes promoted HER kinetics [20,58]. In terms of η_{10} and Tafel slope, the catalytic activity of LA-NiCoP outperforms majority of the reported NCPs electrocatalysts (Fig. 3c and Table S1). In the fitted Nyquist plots (Fig. 3d), the charge transfer resistance (R_{ct}) of LA-NiCoP (42 Ω) is significantly smaller than a-NiCoP (63 Ω) and c-NiCoP (76 Ω), implying its faster charge transfer [59]. To understand the surface property of the samples, the electrochemically active surface area (ECSA) was probed via the double layer capacitance (C_{dl}) method [60,61]. The C_{dl} of LA-NiCoP, a-NiCoP and c-NiCoP are determined to be 45.7, 55.8, and
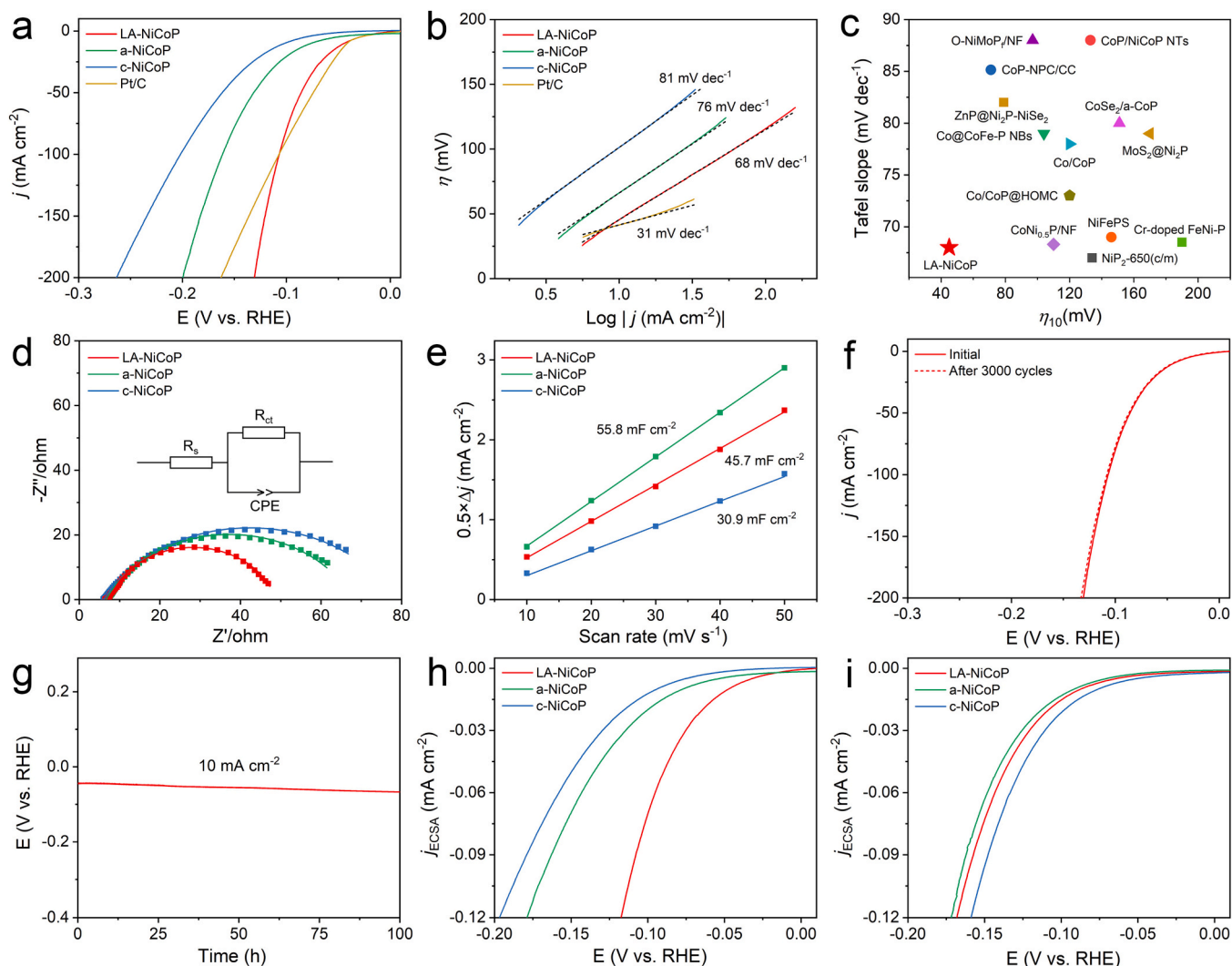
Fig. 3. (a) Polarization curves and (b) Tafel plots of LA-NiCoP, a-NiCoP, c-NiCoP, and Pt/C. (c) Comparison of η_{10} and Tafel slope of LA-NiCoP with the reported NCPs HER electrocatalysts. (d) Nyquist plots of LA-NiCoP, a-NiCoP, and c-NiCoP. (e) Linear plots of double layer current density as a function of the scan rate. (f) Polarization curves of LA-NiCoP before and after 3000 CV cycles. (g) Chronopotentiometry curve of LA-NiCoP recorded at a constant current density of 10 mA cm^{-2}. ECSA-normalized polarization curves of LA-NiCoP, a-NiCoP, and c-NiCoP in (h) alkaline and (i) acidic media.

30.9 mF cm^{-2} (Fig. 3e and S11), respectively. Accordingly, the ECSA is calculated to be 143.5 cm^2 for LA-NiCoP, 175.2 cm^2 for a-NiCoP and 97.0 cm^2 for c-NiCoP, documenting that the introduction of amorphous phase brings more accessible active sites for electrochemical reactions.

The electrochemical stability of LA-NiCoP was first evaluated by repetitive cyclic voltammetry (CV) test. After 3000 CV cycles, the polarization curve shows negligible degradation compared with the initial one (Fig. 3f). In addition, at a constant current density of 10 mA cm^{-2}, the chronopotentiometry measurement of LA-NiCoP proceeds smoothly for 100 h without sharp change (Fig. 3g). After the measurement, LA-NiCoP still retains the massaging ball-like morphology and locally amorphous structure (Fig. S12), verifying its superb structural stability. However, post-mortem XPS analysis demonstrates that the metal–P bonds related Ni 2p$_{3/2}$, Co 2p$_{3/2}$, and P 2p peaks show dramatically decreased intensity, whilst the peak intensities of metal–O exhibit significant enhancement after the stability test (Fig. S13). This is attributed to the surface oxidization of LA-NiCoP during HER [6]. Based on HRTEM analysis, the surface oxidation layer is about 2.0 nm (Fig. S14), which has negligible influence on the electrochemical activity of LA-NiCoP [56,62]. For better clarification, the LA-NiCoP after stability test was soaked in dilute acid to remove the surface oxidized layer. As shown in Fig. S15, the peak intensities of metal–P bonds related Ni 2p$_{3/2}$, Co 2p$_{3/2}$

and P 2p are sharply increased, implying the removal of surface oxidation layer. Meanwhile, the polarization curves of LA-NiCoP before and after acid treatment are almost identical with each other (Fig. S16). Thus, the enhanced alkaline HER activity of LA-NiCoP is mainly ascribed to the locally amorphous structure.

To exclude the geometry effect, the polarization curves of LA-NiCoP, a-NiCoP, and c-NiCoP acquired in 1.0 M KOH are normalized to their ECSA. As revealed in Fig. 3h, LA-NiCoP still exhibits larger current density as compared to a-NiCoP and c-NiCoP, indicating the locally amorphous structure possesses higher intrinsic HER activity than the crystalline one. To identify the particular effect of the locally amorphous structure during alkaline HER, the catalytic behaviors of LA-NiCoP, a-NiCoP, and c-NiCoP in 0.5 M H$_2$SO$_4$ were also investigated for comparison. As shown in Fig. 3i and S17, the geometric activity of LA-NiCoP is better than a-NiCoP and c-NiCoP in acidic media, while the intrinsic activity shows opposite trend. This result demonstrates that local amorphization can improve the acidic HER performance of c-NiCoP by increasing its ECSA instead of the intrinsic activity (Fig. S18). It is commonly believed that the intrinsic HER activity in acidic condition is determined only by H* adsorption capability [4], whereas the intrinsic HER activity in alkaline media is influenced by both H* adsorption and water dissociation kinetics [63,64]. Hence, the significantly enhanced
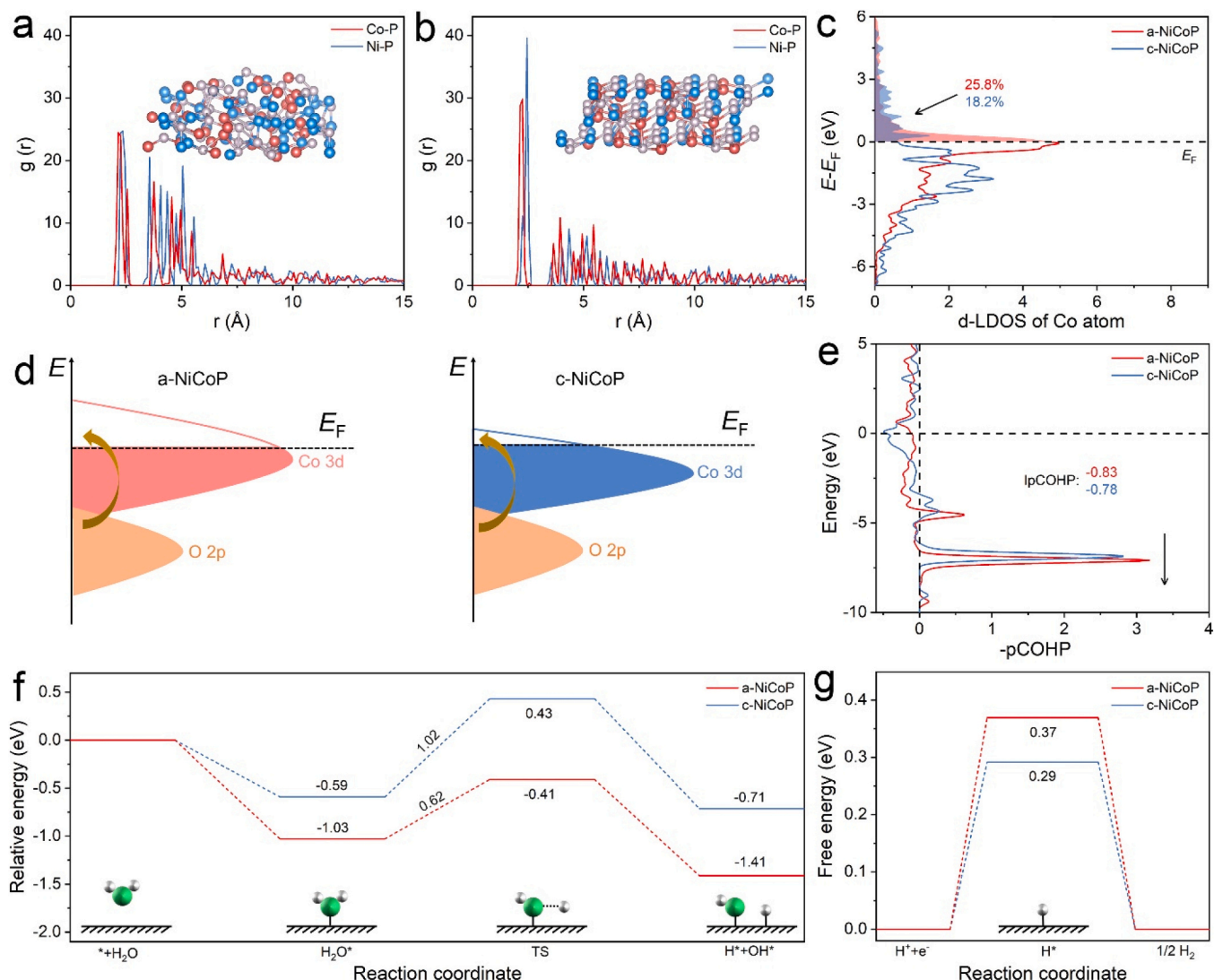
Fig. 4. RDF plots and the corresponding models of (a) a-NiCoP and (b) c-NiCoP. The blue, red and purple balls represent the atoms of Ni, Co and P, respectively. (c) Calculated d-LDOS for Co atom in a-NiCoP and c-NiCoP. (d) Schematic energy bands of H_2O and Co 3d in a-NiCoP and c-NiCoP. E_F represents the Fermi level. (e) pCOHP analysis of Co–O bond on a-NiCoP and c-NiCoP. (f) Calculated energy diagram of water adsorption/dissociation and (g) hydrogen adsorption, where the green and white balls successively represent the atoms of O and H.

intrinsic activity of LA-NiCoP in alkaline media can be attributed to its accelerated water dissociation process.

3.3. Theoretical investigation of LA-NiCoP

To gain further insight into the excellent activity of LA-NiCoP for alkaline HER, DFT calculations were carried out. On the basis of the TEM results, the (111) lattice plane of c-NiCoP was used for simulations, while the model of a-NiCoP was obtained by relaxing c-NiCoP at 1000 K to destroy its ordered atomic arrangement (see the experimental section for details) [5,25,26]. As shown in inset of Fig. 4a and b, the crystal structure of a-NiCoP exhibits distinct randomness compared with c-NiCoP. Moreover, the radial distribution function (RDF) analyses also illustrate that the distance between Ni/Co and P atoms in a-NiCoP possess more uniform distribution than c-NiCoP, which suggests the worse periodicity (Fig. 4a and b) [34,65].

According to previous publications, H_2O molecule tends to be adsorbed on the Co atom in NiCo-based bimetallic HER catalysts due to the lower electronegativity corresponding to a higher positive charge [44]. Thus, the electronic configurations of Co atom in a-NiCoP and c-NiCoP were particularly concerned. As shown in Fig. 4c, the d orbital

local density of states (d-LDOS) analysis demonstrates that the Co atom in a-NiCoP holds a high proportion of unoccupied 3d orbital (25.8 %), far exceeds the Co atom in c-NiCoP (18.2 %). This indicates that the Co atom in the amorphous structure can provide more unoccupied 3d orbitals for accommodating lone pair electrons of O atom in H_2O, thereby resulting in stronger orbital overlap between the Co 3d orbital and O 2p orbital in H_2O (Fig. 4d) [11]. In addition, the projected crystal orbital Hamilton population (pCOHP) analysis was performed to directly reveal the strength of Co–O bonds on different catalysts, in which the positive and negative COHP values are attributed to the bonding and anti-bonding states, respectively [66,67]. The optimized models of water adsorption on a-NiCoP and c-NiCoP are shown in Figs. S19 and S20. Compared with the Co–O bond in c-NiCoP, the bonding states of the Co–O bond in a-NiCoP significantly shift to a lower energy level, while the Co–O bond in a-NiCoP also shows a more negative IpCOHP value (integral of the projected COHP curve below the Fermi level), which suggest a stronger coupling between the Co atom in a-NiCoP and water molecule (Fig. 4e) [10]. Meanwhile, the p orbital local density of states (p-LDOS) of O atom adsorbed on a-NiCoP also shift to the lower energy level than that of c-NiCoP (Fig. S21), further corroborating the favorable water adsorption on the amorphous structure. Consequently, a-NiCoP
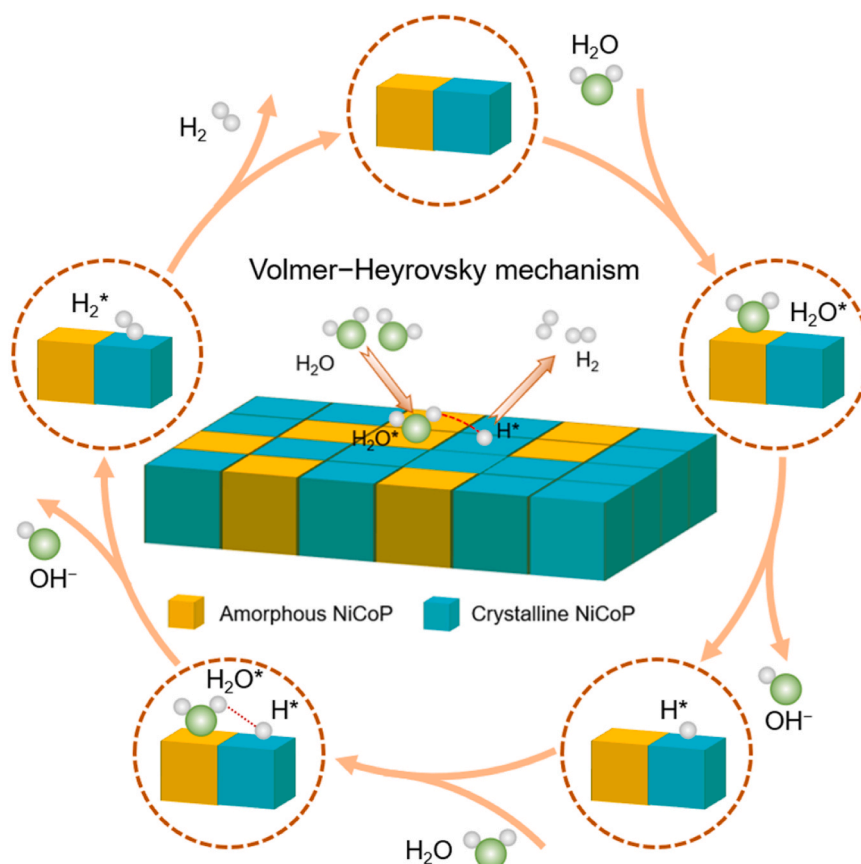
Fig. 5. Schematic diagram of the alkaline HER process in LA-NiCoP.

exhibits a more negative water adsorption free energy of −1.03 eV than c-NiCoP (−0.59 eV), as shown in Fig. 4f. Moreover, the strong coupling between Co atom in a-NiCoP and H_2O molecule can tremendously boost the water dissociation process, which is illustrated by the energy barriers of water dissociation on a-NiCoP (0.62 eV) and c-NiCoP (1.02 eV). The favorable water adsorption and dissociation on Co atom in a-NiCoP indicates that H_2O molecule can be easily activated on the amorphous parts in LA-NiCoP to supply sufficient H* for accelerating alkaline HER.

The adsorption free energy of the hydrogen adsorption (ΔG_{H*}) on the a-NiCoP and c-NiCoP was also investigated. The optimized ΔG_{H*} associated with their adsorption configurations are shown in Fig. 4g and S22, respectively. Unexpectedly, compared with a-NiCoP (0.37 eV), c-NiCoP delivers the optimal ΔG_{H*} value of 0.29 eV that is more closer to zero, revealing that the crystalline regions are more effective for H* adsorption and H_2 evolution [68,69]. The favorable H* adsorption in c-NiCoP can be ascribed to the electron-rich feature due to the lower oxidation state [62]. Nevertheless, opposition trend with LA-NiCoP better than c-NiCoP is obtained in alkaline medium, which is largely associated with the enhanced water dissociation kinetics of amorphous structure in LA-NiCoP. Based on the above experimental and theoretical analyses, a possible reaction mechanism of alkaline HER catalyzed by LA-NiCoP is proposed (Fig. 5). Firstly, water molecule is adsorbed on the amorphous regions in the LA-NiCoP and dissociates into H* and OH⁻ with the aid of one electron by the Volmer process ($H_2O + e^- = H* + OH^-$). Next, the produced H* intermediates are adsorbed on the c-NiCoP for the subsequent reaction because of the optimal ΔG_{H*}. Subsequently, another H_2O molecular, in which OH−H bond is weakened owing to enhanced orbital coupling, interacts with H* adsorbed on the crystalline domains of LA-NiCoP to finish the Heyrovsky reaction ($H_2O + e^- + H* = H_2 + OH^-$). Finally, the desorption of H_2 molecular releases active sites to complete one catalytic cycle. The synergy of a-NiCoP for accelerating water dissociation and c-NiCoP for enhancing H* adsorption makes the LA-NiCoP an outstanding catalyst for alkaline HER.

4. Conclusions

In summary, we have reported a diffusion-limited phase-transition strategy for fabricating locally amorphous NCPs. By using NaH_2PO_2 as the phosphorus source and reaction medium, a unique phosphatization environment with high viscosity is accomplished to impede the diffusion of metal ions and NiCoP units. The sluggish molecular motion results in locally high concentration of NiCoP units, which immediately aggregate to form amorphous phase. Subsequently, the initially formed amorphous phase progressively transforms to more stable crystalline phase, initiating the construction of a locally amorphous structure. Impressively, LA-NiCoP exhibits the best catalytic performance with a low η_{10} of 45 mV and a small Tafel slope of 68 mV dec^{-1} as well as excellent stability for 100 h. The experimental results in combination with theoretical calculations reveal that the amorphous and crystalline phases of LA-NiCoP can cooperate to accelerate the key elementary steps in alkaline HER, during which amorphous phase promotes water dissociation while crystalline phase converts H* to H_2. Moreover, this diffusion-limited phase-transition strategy has also been generalized to fabricate locally amorphous $Ni_{12}P_5$ and Co_2P.

CRediT authorship contribution statement

Ke Wang: Conceptualization, Methodology, Data Curation, Writing-Original Draft; **Song He:** Theoretical calculations, Writing-Original Draft; **Linghai Xie:** Software, Resources; **Tingfeng Wang:** Data Curation, Investigation; **Boxin Li:** Data Curation, Investigation; **Zhuzhu Du:** Data Curation, Investigation; **Hongfang Du:** Supervision, Writing-Review & Editing; **Wei Ai:** Supervision, Funding Acquisition.

Declaration of Competing Interest

The authors declare that they have no known competing financial interests or personal relationships that could have appeared to influence the work reported in this paper.

Data availability

Data will be made available on request.

Acknowledgments

Appendix A. Supporting information

Supplementary data associated with this article can be found in the online version at doi:10.1016/j.apcatb.2023.123136.

References

[1] J. Zhu, L. Hu, P. Zhao, L.Y.S. Lee, K.Y. Wong, Recent advances in electrocatalytic hydrogen evolution using nanoparticles, Chem. Rev. 120 (2020) 851–918, https://doi.org/10.1021/acs.chemrev.9b00248.

[2] S.H. Li, M.Y. Qi, Z.R. Tang, Y.J. Xu, Nanostructured metal phosphides: from controllable synthesis to sustainable catalysis, Chem. Soc. Rev. 50 (2021) 7539–7586, https://doi.org/10.1039/D1CS00323B.

[3] Y. Shi, M. Li, Y. Yu, B. Zhang, Recent advances in nanostructured transition metal phosphides: synthesis and energy-related applications, Energy Environ. Sci. 13 (2020) 4564–4582, https://doi.org/10.1039/D0EE02577A.

[4] D. Cao, B. Sheng, Z. Qi, W. Xu, S. Chen, O.A. Moses, R. Long, Y. Xiong, X. Wu, L. Song, Self-optimizing iron phosphorus oxide for stable hydrogen evolution at high current, Appl. Catal. B 298 (2021), 120559, https://doi.org/10.1016/j.apcatb.2021.120559.

[5] S. Shen, Z. Wang, Z. Lin, K. Song, Q. Zhang, F. Meng, L. Gu, W. Zhong, Crystalline-amorphous interfaces coupling of CoSe₂/CoP with optimized d-Band center and boosted electrocatalytic hydrogen evolution, Adv. Mater. 34 (2022) 2110631, https://doi.org/10.1002/adma.202110631.

[6] H. Yang, P. Guo, R. Wang, Z. Chen, H. Xu, H. Pan, D. Sun, F. Fang, R. Wu, Sequential phase conversion-induced phosphides heteronanorod arrays for superior hydrogen evolution performance to Pt in wide pH media, Adv. Mater. 34 (2022) 2107548, https://doi.org/10.1002/adma.202107548.

[7] H. Zhou, Y. Ren, Z. Li, M. Xu, Y. Wang, R. Ge, X. Kong, L. Zheng, H. Duan, Electrocatalytic upcycling of polyethylene terephthalate to commodity chemicals and H₂ fuel, Nat. Commun. 12 (2021) 4679, https://doi.org/10.1038/s41467-021-25048-x.

[8] B. You, Y. Zhang, Y. Jiao, K. Davey, S.Z. Qiao, Negative charging of transition-metal phosphides via strong electronic coupling for destabilization of alkaline water, Angew. Chem. Int. Ed. 58 (2019) 11796–11800, https://doi.org/10.1002/anie.201906683.

[9] Y. Men, P. Li, J. Zhou, S. Chen, W. Luo, Trends in alkaline hydrogen evolution activity on cobalt phosphide electrocatalysts doped with transition metals, Cell Rep. Phys. Sci. 1 (2020), 100136, https://doi.org/10.1016/j.xcrp.2020.100136.

[10] Y. Men, X. Su, P. Li, Y. Tan, C. Ge, S. Jia, L. Li, J. Wang, G. Cheng, L. Zhuang, S. Chen, W. Luo, Oxygen-inserted top-surface layers of Ni for boosting alkaline hydrogen oxidation electrocatalysis, J. Am. Chem. Soc. 144 (2022) 12661, https://doi.org/10.1021/jacs.2c01448.

[11] Y. Xie, J. Cai, Y. Wu, Y. Zang, X. Zheng, J. Ye, P. Cui, S. Niu, Y. Liu, J. Zhu, X. Liu, G. Wang, Y. Qian, Boosting water dissociation kinetics on Pt–Ni nanowires by N-induced orbital tuning, Adv. Mater. 31 (2019) 1807780, https://doi.org/10.1002/adma.201807780.

[12] Z. Zhou, Y. Kong, H. Tan, Q. Huang, C. Wang, Z. Pei, H. Wang, Y. Liu, Y. Wang, S. Li, X. Liao, W. Yan, S. Zhao, Cation-vacancy-enriched nickel phosphide for efficient electrosynthesis of hydrogen peroxides, Adv. Mater. 34 (2022) 2106541, https://doi.org/10.1002/adma.202106541.

[13] Y. Li, Z. Dong, L. Jiao, Multifunctional transition metal-based phosphides in energy-related electrocatalysis, Adv. Energy Mater. 10 (2020) 1902104, https://doi.org/10.1002/aenm.201902104.

[14] Z. Pu, T. Liu, I.S. Amiinu, R. Cheng, P. Wang, C. Zhang, P. Ji, W. Hu, J. Liu, S. Mu, Transition-metal phosphides: activity origin, energy-related electrocatalysis applications, and synthetic strategies, Adv. Funct. Mater. 30 (2020) 2004009, https://doi.org/10.1002/adfm.202004009.

[15] H. Du, Z. Du, T. Wang, B. Li, S. He, K. Wang, L. Xie, W. Ai, W. Huang, Unlocking interfacial electron transfer of ruthenium phosphides by homologous core–shell design toward efficient hydrogen evolution and oxidation, Adv. Mater. 34 (2022) 2204624, https://doi.org/10.1002/adma.202204624.

[16] Z. Yu, Y. Duan, X. Feng, X. Yu, M. Gao, S. Yu, Clean and affordable hydrogen fuel from alkaline water splitting: past, recent progress, and future prospects, Adv. Mater. 33 (2021) 2007100, https://doi.org/10.1002/adma.202007100.

[17] K. Xu, H. Cheng, H. Lv, J. Wang, L. Liu, S. Liu, X. Wu, W. Chu, C. Wu, Y. Xie, Controllable surface reorganization engineering on cobalt phosphide nanowire arrays for efficient alkaline hydrogen evolution reaction, Adv. Mater. 30 (2018) 1703322, https://doi.org/10.1002/adma.201703322.

[18] J. Huang, J. Han, T. Wu, K. Feng, T. Yao, X. Wang, S. Liu, J. Zhong, Z. Zhang, Y. Zhang, B. Song, Boosting hydrogen transfer during volmer reaction at oxides/metal nanocomposites for efficient alkaline hydrogen evolution, ACS Energy Lett. 4 (2019) 3002–3010, https://doi.org/10.1021/acsenergylett.9b02359.

[19] L.W. Jiang, Y. Huang, Y. Zou, C. Meng, Y. Xiao, H. Liu, J.J. Wang, Boosting the stability of oxygen vacancies in α-Co(OH)₂ nanosheets with coordination polyhedrons as rivets for high-performance alkaline hydrogen evolution electrocatalyst, Adv. Energy Mater. 12 (2022) 2202351, https://doi.org/10.1002/aenm.202202351.

[20] H. Sun, Z. Yan, C. Tian, C. Li, X. Feng, R. Huang, Y. Lan, J. Chen, C.P. Li, Z. Zhang, M. Du, Bixbyite-type Ln₂O₃ as promoters of metallic Ni for alkaline electrocatalytic hydrogen evolution, Nat. Commun. 13 (2022) 3857, https://doi.org/10.1038/s41467-022-31561-4.

[21] Q. He, D. Tian, H. Jiang, D. Cao, S. Wei, D. Liu, P. Song, Y. Lin, L. Song, Achieving efficient alkaline hydrogen evolution reaction over a Ni₅P₄ catalyst incorporating single-atomic Ru sites, Adv. Mater. 32 (2020) 1906972, https://doi.org/10.1002/adma.201906972.

[22] H. Song, M. Wu, Z. Tang, J.S. Tse, B. Yang, S. Lu, Single atom ruthenium-doped CoP/CDs nanosheets via splicing of carbon-dots for robust hydrogen production, Angew. Chem. Int. Ed. 60 (2021) 7234–7244, https://doi.org/10.1002/anie.202017102.

[23] J. Xu, T. Liu, J. Li, B. Li, Y. Liu, B. Zhang, D. Xiong, I. Amorim, W. Li, L. Liu, Boosting the hydrogen evolution performance of ruthenium clusters through synergistic coupling with cobalt phosphide, Energy Environ. Sci. 11 (2018) 1819–1827, https://doi.org/10.1039/C7EE03603E.

[24] G. Zhao, K. Rui, S. Dou, W. Sun, Heterostructures for electrochemical hydrogen evolution reaction: a review, Adv. Funct. Mater. 28 (2018) 1803291, https://doi.org/10.1002/adfm.201803291.

[25] J. Wang, L. Han, B. Huang, Q. Shao, H.L. Xin, X. Huang, Amorphization activated ruthenium-tellurium nanorods for efficient water splitting, Nat. Commun. 10 (2019) 5692, https://doi.org/10.1038/s41467-019-13519-1.

[26] Y. He, L. Liu, C. Zhu, S. Guo, P. Golani, B. Koo, P. Tang, Z. Zhao, M. Xu, C. Zhu, P. Yu, X. Zhou, C. Gao, X. Wang, Z. Shi, L. Zheng, J. Yang, B. Shin, J. Arbiol, H. Duan, Y. Du, M. Heggen, R.E. Dunin-Borkowski, W. Guo, Q.J. Wang, Z. Zhang, Z. Liu, Amorphizing noble metal chalcogenide catalysts at the single-layer limit towards hydrogen production, Nat. Catal. 5 (2022) 212–221, https://doi.org/10.1038/s41929-022-00753-y.

[27] F.-Y. Gao, S.-N. Liu, J.-C. Ge, X.-L. Zhang, L. Zhu, Y.-R. Zheng, Y. Duan, S. Qin, W. Dong, X. Yu, R.-C. Bao, P.-P. Yang, Z.-Z. Niu, Z.-G. Ding, W. Liu, S. Lan, M.-R. Gao, Y. Yan, S.-H. Yu, Nickel–molybdenum–niobium metallic glass for efficient hydrogen oxidation in hydroxide exchange membrane fuel cells, Nat. Catal. 5 (2022) 993–1005, https://doi.org/10.1038/s41929-022-00862-8.

[28] S. He, H. Du, K. Wang, Q. Liu, J. Sun, Y. Liu, Z. Du, L. Xie, W. Ai, W. Huang, Low-temperature molten salt synthesis of MoS₂@CoS₂ heterostructures for efficient hydrogen evolution reaction, Chem. Commun. 56 (2020) 5548–5551, https://doi.org/10.1039/D0CC01726D.

[29] G. Kresse, J. Furthmüller, Efficient iterative schemes for ab initio total-energy calculations using a plane-wave basis set, Phys. Rev. B 54 (1996) 11169–11186, https://doi.org/10.1103/PhysRevB.54.11169.

[30] J.P. Perdew, K. Burke, M. Ernzerhof, Generalized gradient approximation made simple, Phys. Rev. Lett. 77 (1996) 3865–3868, https://doi.org/10.1103/PhysRevLett.77.3865.

[31] L. Huang, Z. Hu, H. Jin, J. Wu, K. Liu, Z. Xu, J. Wan, H. Zhou, J. Duan, B. Hu, J. Zhou, Salt-assisted synthesis of 2D materials, Adv. Funct. Mater. 30 (2020) 1908486, https://doi.org/10.1002/adfm.201908486.

[32] R. Li, R. Wu, Z. Li, J. Wang, X. Liu, Y. Wen, F.-K. Chiang, S.-W. Chen, K.C. Chan, Z. Lu, Boosting oxygen-evolving activity via atom-stepped interfaces architected with kinetic frustration, Adv. Mater. 34 (2022) 2206890, https://doi.org/10.1002/adma.202206890.

[33] F. Swallen Stephen, L. Kearns Kenneth, K. Mapes Marie, S. Kim Yong, J. McMahon Robert, M.D. Ediger, T. Wu, L. Yu, S. Satija, Organic glasses with exceptional thermodynamic and kinetic stability, Science 315 (2007) 353–356, https://doi.org/10.1126/science.1135795.

[34] G. Wu, X. Zheng, P. Cui, H. Jiang, X. Wang, Y. Qu, W. Chen, Y. Lin, H. Li, X. Han, Y. Hu, P. Liu, Q. Zhang, J. Ge, Y. Yao, R. Sun, Y. Wu, L. Gu, X. Hong, Y. Li, A general synthesis approach for amorphous noble metal nanosheets, Nat. Commun. 10 (2019) 4855, https://doi.org/10.1038/s41467-019-12859-2.

[35] X. Chen, A.C.S. Samia, Y. Lou, C. Burda, Investigation of the crystallization process in 2 nm CdSe quantum dots, J. Am. Chem. Soc. 127 (2005) 4372–4375, https://doi.org/10.1021/ja0458219.

[36] J. Lee, J. Yang, S.G. Kwon, T. Hyeon, Nonclassical nucleation and growth of inorganic nanoparticles, Nat. Rev. Mater. 1 (2016) 16034, https://doi.org/10.1038/natrevmats.2016.34.

[37] J.F. Lutsko, How crystals form: a theory of nucleation pathways, Sci. Adv. 5 (2019) eaav7399, https://doi.org/10.1126/sciadv.aav7399.

[38] W. Li, F. Li, H. Yang, X. Wu, P. Zhang, Y. Shan, L. Sun, A bio-inspired coordination polymer as outstanding water oxidation catalyst via second coordination sphere engineering, Nat. Commun. 10 (2019) 5074, https://doi.org/10.1038/s41467-019-13052-1.

[39] J.L. MacManus-Driscoll, S.C. Wimbush, Processing and application of high-temperature superconducting coated conductors, Nat. Rev. Mater. 6 (2021) 587–604, https://doi.org/10.1038/s41578-021-00290-3.

[40] T.H. Zhang, X.Y. Liu, How does a transient amorphous precursor template crystallization, J. Am. Chem. Soc. 129 (2007) 13520–13526, https://doi.org/10.1021/ja073598k.

[41] E. Hu, Y. Feng, J. Nai, D. Zhao, Y. Hu, X.W. Lou, Construction of hierarchical Ni–Co–P hollow nanobricks with oriented nanosheets for efficient overall water splitting, Energy Environ. Sci. 11 (2018) 872–880, https://doi.org/10.1039/C8EE00076J.

[42] Z. Fang, L. Peng, Y. Qian, X. Zhang, Y. Xie, J.J. Cha, G. Yu, Dual tuning of Ni–Co–A (A = P, Se, O) nanosheets by anion substitution and holey engineering for efficient hydrogen evolution, J. Am. Chem. Soc. 140 (2018) 5241–5247, https://doi.org/10.1021/jacs.8b01548.

[43] R. Sun, Y. Bai, Z. Bai, L. Peng, M. Luo, M. Qu, Y. Gao, Z. Wang, W. Sun, K. Sun, Phosphorus vacancies as effective polysulfide promoter for high-energy-density lithium–sulfur batteries, Adv. Energy Mater. 12 (2022) 2102739, https://doi.org/10.1002/aenm.202102739.

[44] Y. Liu, X. Liu, A.R. Jadhav, T. Yang, Y. Hwang, H. Wang, L. Wang, Y. Luo, A. Kumar, J. Lee, H.T.D. Bui, M. Gyu Kim, H. Lee, Unraveling the function of metal–amorphous support interactions in single-atom electrocatalytic hydrogen evolution, Angew. Chem. Int. Ed. 61 (2022) 202114160, https://doi.org/10.1002/anie.202114160.

[45] K. Wang, H. Du, S. He, L. Liu, K. Yang, J. Sun, Y. Liu, Z. Du, L. Xie, W. Ai, W. Huang, Kinetically controlled, scalable synthesis of γ-FeOOH nanosheet arrays on nickel foam toward efficient oxygen evolution: the key role of in-situ-generated γ-NiOOH, Adv. Mater. 33 (2021) 2005587, https://doi.org/10.1002/adma.202005587.

[46] S. Yang, J.-Y. Zhu, X.-N. Chen, M.-J. Huang, S.-H. Cai, J.-Y. Han, J.-S. Li, Self-supported bimetallic phosphides with artificial heterointerfaces for enhanced electrochemical water splitting, Appl. Catal. B 304 (2022), 120914, https://doi.org/10.1016/j.apcatb.2021.120914.

[47] L. Huang, R. Yao, X. Wang, S. Sun, X. Zhu, X. Liu, M.G. Kim, J. Lian, F. Liu, Y. Li, H. Zong, S. Han, X. Ding, In situ phosphating of Zn-doped bimetallic skeletons as a versatile electrocatalyst for water splitting, Energy Environ. Sci. 15 (2022) 2425–2434, https://doi.org/10.1039/D1EE02764F.

[48] A. Li, L. Zhang, F. Wang, L. Zhang, L. Li, H. Chen, Z. Wei, Rational design of porous Ni-Co-Fe ternary metal phosphides nanobricks as bifunctional electrocatalysts for efficient overall water splitting, Appl. Catal. B 310 (2022) 121353, https://doi.org/10.1016/j.apcatb.2022.121353.

[49] Y. Men, Y. Tan, P. Li, X. Cao, S. Jia, J. Wang, S. Chen, W. Luo, Tailoring the 3d-orbital electron filling degree of metal center to boost alkaline hydrogen evolution electrocatalysis, Appl. Catal. B 284 (2021), 119718, https://doi.org/10.1016/j.apcatb.2020.119718.

[50] Y. Hu, L. Li, J. Zhao, Y.-C. Huang, C.-y Kuo, J. Zhou, Y. Fan, H.-J. Lin, C.-L. Dong, C.-W. Pao, J.-F. Lee, C.-T. Chen, C. Jin, Z. Hu, J.-Q. Wang, L. Zhang, Large current density for oxygen evolution from pyramidally-coordinated Co oxide, Appl. Catal. B 333 (2023), 122785, https://doi.org/10.1016/j.apcatb.2023.122785.

[51] B. Cao, Y. Cheng, M. Hu, P. Jing, Z. Ma, B. Liu, R. Gao, J. Zhang, Efficient and durable 3D self-supported nitrogen-doped carbon-coupled nickel/cobalt phosphide electrodes: stoichiometric ratio regulated phase- and morphology-dependent overall water splitting performance, Adv. Funct. Mater. 29 (2019) 1906316, https://doi.org/10.1002/adfm.201906316.

[52] J. Sun, Y. Liu, L. Liu, S. He, Z. Du, K. Wang, L. Xie, H. Du, W. Ai, Expediting sulfur reduction/evolution reactions with integrated electrocatalytic network: a comprehensive kinetic map, Nano Lett. 22 (2022) 3728–3736, https://doi.org/10.1021/acs.nanolett.2c00642.

[53] N. Yang, H. Cheng, X. Liu, Q. Yun, Y. Chen, B. Li, B. Chen, Z. Zhang, X. Chen, Q. Lu, J. Huang, Y. Huang, Y. Zong, Y. Yang, L. Gu, H. Zhang, Amorphous/crystalline hetero-phase Pd nanosheets: one-pot synthesis and highly selective hydrogenation reaction, Adv. Mater. 30 (2018) 1803234, https://doi.org/10.1002/adma.201803234.

[54] Y. Wu, Y. Zhao, P. Zhai, C. Wang, J. Gao, L. Sun, J. Hou, Triggering lattice oxygen activation of single-atomic Mo sites anchored on Ni–Fe oxyhydroxides nanoarrays for electrochemical water oxidation, Adv. Mater. 34 (2022) 2202523, https://doi.org/10.1002/adma.202202523.

[55] Y. Li, H. Wang, L. Xie, Y. Liang, G. Hong, H. Dai, MoS2 nanoparticles grown on graphene: an advanced catalyst for the hydrogen evolution reaction, J. Am. Chem. Soc. 133 (2011) 7296–7299, https://doi.org/10.1021/ja201269b.

[56] T. Liu, A. Li, C. Wang, W. Zhou, S. Liu, L. Guo, Interfacial electron transfer of Ni2P–NiP2 polymorphs inducing enhanced electrochemical properties, Adv. Mater. 30 (2018) 1803590, https://doi.org/10.1002/adma.201803590.

[57] C. Lei, Y. Wang, Y. Hou, P. Liu, J. Yang, T. Zhang, X. Zhuang, M. Chen, B. Yang, L. Lei, C. Yuan, M. Qiu, X. Feng, Efficient alkaline hydrogen evolution on atomically dispersed Ni–Nx Species anchored porous carbon with embedded Ni nanoparticles by accelerating water dissociation kinetics, Energy Environ. Sci. 12 (2019) 149–156, https://doi.org/10.1039/C8EE01841C.

[58] X. Wang, J. Sun, T. Li, Z. Song, D. Wu, B. Zhao, K. Xiang, W. Ai, X.-Z. Fu, J.-L. Luo, Folic acid self-assembly synthesis of ultrathin N-doped carbon nanosheets with single-atom metal catalysts, Energy Storage Mater. 36 (2021) 409–416, https://doi.org/10.1016/j.ensm.2021.01.024.

[59] M. Wei, Y. Sun, F. Ai, S. Xi, J. Zhang, J. Wang, Stretchable high-entropy alloy nanoflowers enable enhanced alkaline hydrogen evolution catalysis, Appl. Catal. B 334 (2023), 122814, https://doi.org/10.1016/j.apcatb.2023.122814.

[60] C. Wei, S. Sun, D. Mandler, X. Wang, S.Z. Qiao, Z.J. Xu, Approaches for measuring the surface areas of metal oxide electrocatalysts for determining their intrinsic electrocatalytic activity, Chem. Soc. Rev. 48 (2019) 2518–2534, https://doi.org/10.1039/C8CS00848E.

[61] Y. Han, H. Duan, W. Liu, C. Zhou, B. Wang, Q. Jiang, S. Feng, W. Yan, T. Tan, R. Zhang, Engineering the electronic structure of platinum single-atom sites via tailored porous carbon nanofibers for large-scale hydrogen production, Appl. Catal. B 335 (2023), 122898, https://doi.org/10.1016/j.apcatb.2023.122898.

[62] Q. Fu, X. Wang, J. Han, J. Zhong, T. Zhang, T. Yao, C. Xu, T. Gao, S. Xi, C. Liang, L. Xu, P. Xu, B. Song, Phase-junction electrocatalysts towards enhanced hydrogen evolution reaction in alkaline media, Angew. Chem. Int. Ed. 60 (2021) 259–267, https://doi.org/10.1002/anie.202011318.

[63] F. Cheng, X. Peng, L. Hu, B. Yang, Z. Li, C.L. Dong, J.L. Chen, L.C. Hsu, L. Lei, Q. Zheng, M. Qiu, L. Dai, Y. Hou, Accelerated water activation and stabilized metal-organic framework via constructing triangular active-regions for ampere-level current density hydrogen production, Nat. Commun. 13 (2022) 6486, https://doi.org/10.1038/s41467-022-34278-6.

[64] G. Wu, X. Han, J. Cai, P. Yin, P. Cui, X. Zheng, H. Li, C. Chen, G. Wang, X. Hong, In-plane strain engineering in ultrathin noble metal nanosheets boosts the intrinsic electrocatalytic hydrogen evolution activity, Nat. Commun. 13 (2022) 4200, https://doi.org/10.1038/s41467-022-31971-4.

[65] W. Ai, X. Cao, Z. Sun, J. Jiang, Z. Du, L. Xie, Y. Wang, X. Wang, H. Zhang, W. Huang, T. Yu, Redox-crosslinked graphene networks with enhanced electrochemical capacitance, J. Mater. Chem. A 2 (2014) 12924–12930, https://doi.org/10.1039/C4TA01309C.

[66] F. Xiao, Y. Wang, G.-L. Xu, F. Yang, S. Zhu, C.-J. Sun, Y. Cui, Z. Xu, Q. Zhao, J. Jang, X. Qiu, E. Liu, W.S. Drisdell, Z. Wei, M. Gu, K. Amine, M. Shao, Fe–N–C boosts the stability of supported platinum nanoparticles for fuel cells, J. Am. Chem. Soc. 144 (2022) 20372–20384, https://doi.org/10.1021/jacs.2c08305.

[67] L. Zeng, Z. Zhao, F. Lv, Z. Xia, S.Y. Lu, J. Li, K. Sun, K. Wang, Y. Sun, Q. Huang, Y. Chen, Q. Zhang, L. Gu, G. Lu, S. Guo, Anti-dissolution Pt single site with Pt(OH)(O3)/Co(P) coordination for efficient alkaline water splitting electrolyzer, Nat. Commun. 13 (2022) 3822, https://doi.org/10.1038/s41467-022-31406-0.

[68] Q. Wu, W. Yang, X. Wang, W. Zhu, S. Lv, Y. Zhou, T. Chen, S. Liu, W. Li, Z. Chen, Inherent vacancy of compressive Ru nanoparticles accelerate electro-catalytic hydrogen energy conversion, Appl. Catal. B 335 (2023), 122896, https://doi.org/10.1016/j.apcatb.2023.122896.

[69] Y. Zhao, N. Jia, X.-R. Wu, F.-M. Li, P. Chen, P.-J. Jin, S. Yin, Y. Chen, Rhodium phosphide ultrathin nanosheets for hydrazine oxidation boosted electrochemical water splitting, Appl. Catal. B 270 (2020), 118880, https://doi.org/10.1016/j.apcatb.2020.118880.